

Electrochemical stability of ZnMn_2O_4 : Understanding Zn-ion rechargeable battery capacity and degradation

Oleg Rubel,^{1,*} Thuy Nguyen Thanh Tran,^{2,3} Storm Gourley,⁴ Sriram Anand,^{1,5}
Andrew Van Bommel,³ Brian D. Adams,³ Douglas G. Ivey,² and Drew Higgins^{4,†}

¹*Department of Materials Science and Engineering,
McMaster University, 1280 Main Street West,
Hamilton, Ontario L8S 4L8, Canada*

²*Department of Chemical and Materials Engineering,
University of Alberta, 9211 116 Street NW,
Edmonton, Alberta, Canada T6G 1H9*

³*Salient Energy Inc., 21 McCurdy Ave,
Dartmouth, Nova Scotia, Canada B3B 1C4*

⁴*Department of Chemical Engineering,
McMaster University, 1280 Main Street West,
Hamilton, Ontario, Canada L8S 4L8*

⁵*Department of Metallurgical and Materials Engineering,
National Institute of Technology Tiruchirappalli, Tamil Nadu 620015, India*

(Dated: March 22, 2022)

Abstract

We present a refined Mn–Zn–H₂O Pourbaix diagram with the emphasis on parameters relevant for the Zn/MnO₂ rechargeable cells. It maps out boundaries of electrochemical stability for MnO₂, ZnMn₂O₄, ZnMn₃O₇, and MnOOH. The diagram helps to rationalize experimental observation on processes and phases occurring during charge/discharge, including the position of charge/discharge redox peaks and capacity fade observed in rechargeable aqueous Zn-ion batteries for stationary storage. The proposed Pourbaix diagram is validated by observing the pH-dependent transformation of electrolytic manganese dioxide to hetaerolite and chalcophanite during discharge and charge, respectively. Our results can guide the selection of operating conditions (the potential range and pH) for existing aqueous Zn/MnO₂ rechargeable cells to maximise their longevity. In addition, the relation between electrochemical stability boundaries and operating conditions can be used as an additional design criterion in exploration of future cathode materials for aqueous rechargeable batteries.

I. INTRODUCTION

Eco-friendly rechargeable Zn-ion batteries with aqueous electrolyte have emerged as a cheaper and safer alternative to Li-ion batteries for certain applications such as grid scale energy storage [1]. In the first realization of an aqueous rechargeable Zn-ion battery, MnO₂ was used as the cathode (positive electrode) material [2]. Since then, polymorphs of MnO₂ remain a material of choice for fabrication of practical cells in spite of a variety of alternative positive electrode materials reported to date [1]. Reversible Zn²⁺ intercalation/deintercalation (discharging/charging) in the MnO₂ host framework and formation of ZnMn₂O₄ [3] combined with H⁺ co-intercalation [4, 5] are recognized as the main energy storage mechanisms in Zn/MnO₂ cells.

Cycling performance of the Zn/MnO₂ cell is limited by capacity fade, especially at slower cycling rates [6] that are necessary for grid-scale energy storage applications. This capacity fade is attributed to dissolution of the active cathode material into the electrolyte (formation of Mn²⁺(aq) [7–9]) as well as the formation of irreversible phases at the cathode side, such

* O.R. email: rubelo@mcmaster.ca, ORCID: 0000-0001-5104-5602

† D.H. email: higgid2@mcmaster.ca, ORCID: 0000-0002-0585-2670

as $\text{Mn}(\text{OH})_2$, Mn_3O_4 or even ZnMn_2O_4 [10]. Current literature is ambiguous about the electrode potential where the dissolution takes place. For instance, Chao *et al.* [11] suggested that Mn^{2+} leaches at high voltages (greater than 1.7 V vs $\text{Zn}^0/\text{Zn}^{2+}$). On the other hand, Li *et al.* [6] attributed capacity fade to reactions that take place at lower voltages (less than 1.26 V vs $\text{Zn}^0/\text{Zn}^{2+}$). It seems that another solid phase $\text{ZnMn}_3\text{O}_7 \cdot n\text{H}_2\text{O}$ (chalcophanite) is also involved in capacity fade [6]. After the initial discharge process, the formation of chalcophanite was observed using X-ray diffraction, and the diffraction peaks associated with this phase became more intense as the cycle number increased, especially at slower cycle rates [6]. Finally, Li *et al.* [6] associated the formation of $\text{ZnMn}_3\text{O}_7 \cdot n\text{H}_2\text{O}$ and Mn_3O_4 below 1.26 V vs $\text{Zn}^0/\text{Zn}^{2+}$ with capacity fade at slow cycling rates. Tran *et al.* [12] also reported $\text{ZnMn}_3\text{O}_7 \cdot 3\text{H}_2\text{O}$ in *ex situ* studies of Zn/EMD cells (EMD stands for electrolytic manganese dioxide [11]) and linked the formation of chalcophanite with the electrochemical deposition of dissolved Mn^{2+} back on the cathode surface during charging at higher voltages (1.8 V vs $\text{Zn}^0/\text{Zn}^{2+}$).

While battery operation is governed by non-equilibrium kinetic processes, understanding which phases of the Mn–Zn– H_2O system are stable within the range of parameters relevant for operation of rechargeable batteries will be important for explaining current stability limitations and designing electrode structures that can provide extended operational lifetimes. In this sense, for aqueous batteries Pourbaix diagrams can be useful for displaying the equilibrium electrochemical stability of a metal– H_2O system. For example, Bischoff *et al.* [13] created an overlay of Mn– H_2O and Zn– H_2O Pourbaix diagrams and measured *in situ* local changes in pH (3 – 5) during the battery cycle within the relevant range of the potential window 0.9 – 1.9 V vs $\text{Zn}^0/\text{Zn}^{2+}$. This diagram allows for several important conclusions: (i) MnO_2 and Mn_2O_3 are the only solid phases of the Mn– H_2O system that are stable in the range specified, (ii) at higher potentials (greater than 1.7 V vs $\text{Zn}^0/\text{Zn}^{2+}$) the only danger is electrolyte decomposition (via the O_2 evolution reaction) and not cathode dissolution, (iii) during discharge there is a problematic region (below ca. 1 V vs $\text{Zn}^0/\text{Zn}^{2+}$ at pH 5.5) where $\text{Mn}^{2+}(\text{aq})$ is more stable than solid MnO_2 . However, the diagram presented by Bischoff *et al.* [13] does not consider stability boundaries of two important solids: hetaerolite ZnMn_2O_4 and chalcophanite $\text{ZnMn}_3\text{O}_7 \cdot 3\text{H}_2\text{O}$.

Huang *et al.* [14] proposed a ternary Mn–Zn– H_2O Pourbaix diagram, yet it does not have many details in the electrochemical potential region of interest for Zn-ion batteries.

Qualitatively, the diagram shows the existence of ZnMn_2O_4 and $\text{Zn}_2\text{Mn}_3\text{O}_8$, but does not present clear boundaries for those phases. Also, $\text{ZnMn}_3\text{O}_7 \cdot 3\text{H}_2\text{O}$ does not appear on this diagram even though it was extensively discussed in the text of Ref. 14. It remains unclear what role these Zn-containing phases play in energy storage with respect to the operation of rechargeable Zn-ion batteries with aqueous electrolyte.

To elucidate the electrochemical stability of ZnMn_2O_4 , we have provided detailed Mn–Zn– H_2O Pourbaix analysis focusing on the relevant range of parameters that are encountered in state of the art rechargeable Zn-ion batteries employing a Zn-sulfate electrolyte [13]: namely, pH 4 – 6 and $E_{\text{Zn}^0/\text{Zn}^{2+}} = 1.1 - 1.8$ V. The new diagram outlines the electrochemical potential and pH regions of ZnMn_2O_4 , $\text{ZnMn}_3\text{O}_7 \cdot 3\text{H}_2\text{O}$, and MnOOH stability. Conclusions drawn from the Pourbaix diagram are corroborated by experimental measurements of the cyclic performance of Zn/EMD cells at variable discharge potentials combined with *ex situ* studies of the cathode material, which provides critical fundamental insight to help understand the stability limitations of conventional electrode structures and guide improved material designs or operational parameters.

II. METHODS

A. Pourbaix diagram

Even though construction of Pourbaix diagrams based on electronic structure calculations has become increasingly accurate [15–18], it is still not fully *ab initio* (mostly hindered by correlation effects of transition metals and finite-temperature thermodynamic properties). Here we build the Pourbaix diagram based on experimental data following the method established by Pourbaix [19] and use a density functional theory (DFT) only when there are no experimental data. A key ingredient for construction of Pourbaix diagrams is standard chemical potentials μ° of species, listed in Table I at standard conditions per formula unit (f.u.).

In our calculations we assume concentrations of aqueous species at 2 M for Zn^{2+} and 0.1 M for Mn^{2+} . These values are based upon typical concentrations of ZnSO_4 and MnSO_4 used in experimental Zn-ion battery research [7, 9, 13]. The concentration of aqueous species

TABLE I. Chemical potentials of species involved in reactions. Bold font highlights primary values used in calculations in the case of multiple values reported in the literature.

Species	μ° (eV/f.u.)	Ref.
Zn ²⁺ (aq)	-1.526	[19]
Mn ²⁺ (aq)	-2.359	[19]
MnO ₄ ⁻ (aq)	-4.657	[19]
H ₂ O (l)	-2.458	[19]
MnO ₂ (pyrolusite)	-4.83	[20]
MnOOH (manganite)	-5.81	estimated from $E^\circ = 0.98$ V at pH 0 [21]
	-5.88	[14, Table S7 in supp. inf.]
ZnO	-3.292	[22]
ZnO hydr.	-3.336	[19]
α -Mn ₂ O ₃	-9.206	[19]
ZnMn ₂ O ₄ (hetaerolite)	-12.61	[23]
	-12.72	[14, supp. inf.]
ZnMn ₃ O ₇ (chalcophanite) hydr.	$-17.83 - \delta\mu$	$\mu^\circ(\text{ZnO hydr.}) + 3\mu^\circ(\text{MnO}_2) - \delta\mu$

is taken into account when computing their chemical potential (eV), e.g.,

$$\mu(\text{Mn}^{2+}) = \mu^\circ(\text{Mn}^{2+}) + 0.0592 \log_{10}[\text{Mn}^{2+}], \quad (1)$$

where $[\text{Mn}^{2+}]$ is the aqueous concentration of Mn²⁺ ions. Sample calculations are presented in the Appendix. It should be noted that experiments in this paper were performed using an electrolyte with 1 M concentration of ZnSO₄ (see Sec. II C). This discrepancy has a minor effect on the calculated Pourbaix diagram and does not affect the main conclusions.

B. Electronic structure calculations

DFT [24, 25] calculations were performed using the Vienna *ab initio* simulation package [26] (VASP) and projector augmented-wave potentials [26–28]. The following potentials were used: Mn_sv, Zn, O_h, H_h. A Perdew-Burke-Ernzerhof [29] (PBE) generalized gradient approximation (GGA) for the exchange-correlation functional was chosen in combination

with the Grimme *et al.* [30] (D3) correction to capture long-range van der Waals interactions.

A full structural relaxation was conducted for all simulated compounds, which included relaxation of atomic positions (maximum Cartesian force component of 0.05 eV/Å) and stresses (1 kBar as the maximum component of the stress tensor). A cutoff energy of $E_{\text{cut}} = 875$ eV for the plane-wave expansion was used, which corresponds to the maximum value recommended in pseudopotential files further increased by 25% above (VASP tag `PREC = High`). The Brillouin zone was sampled using a Monkhorst and Pack [31] shifted k mesh with a density of 20 divisions for every 1 Å⁻¹ linear dimension in reciprocal space.

Magnetism was included for structures with manganese and the O₂ molecule. In the O₂ molecule the ordering is ferromagnetic. We tested all possible permutations of antiferromagnetic arrangements in addition to the ferromagnetic ordering for structures with manganese and selected the lowest total energy.

C. Electrode fabrication

EMD was obtained from Borman Specialty Materials (formerly Tronox). All chemicals were used as received without further purification. A proprietary slurry cast method was used to prepare EMD electrodes [32]. The Zn-ion battery cells were made from a frame of acrylic sheets and Ti current collectors. The Zn electrode was positioned on top of the cell and separated from the underlying MnO₂ electrode by three layers of filter paper soaked with the electrolyte. The contact area between the electrodes and the electrolyte was 4 cm².

Deionized water was used to prepare the electrolyte solutions. 1 M ZnSO₄ solutions with pH 2.5 and pH 4 were used as the electrolyte for the zinc-ion batteries. H₂SO₄ was used to adjust the pH of the zinc sulfate electrolytes.

D. Characterization of EMD electrodes and electrochemical testing

The morphologies and compositions of the EMD electrodes were characterized using a scanning electron microscope (Tescan Vega3 SEM), coupled with an energy dispersive X-ray (EDX) spectrometer. X-ray diffraction (XRD) analysis was performed using a Rigaku Ultima IV diffractometer with monochromatic Cu K α X-radiation (wavelength equal to 1.54 Å) at a scan rate of 5 degrees min⁻¹. Transmission electron microscopy (TEM) and

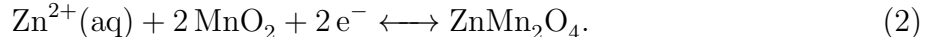
selected area electron diffraction (SAED) were performed using a JEOL JEM-ARM200CF TEM/STEM operating at an accelerating voltage of 200 kV.

Electrochemical measurements were carried out with a Biologic SP-300 potentiostat. Batteries were first conditioned at a C-rate of C/10 and cycled at C/5. During the charging process, the batteries were held at 1.8 V for an additional 2 h or until the current density dropped to $8 \mu\text{A mg}^{-1}$, whichever came first.

III. RESULTS AND DISCUSSION

A. Electrochemical stability of hetaerolite and Zn^{2+} -related energy storage

We began construction of the Mn–Zn–H₂O Pourbaix diagram by mapping out a region of stability for ZnMn_2O_4 (hetaerolite) as the only structure of MnO_2 with intercalated Zn for which thermodynamic properties are known. The charge and discharge of this structure with divalent Zn^{2+} ions is the key fundamental process occurring during rechargeable battery operation, which is governed by the reaction



Since there are no protons involved in this reaction, its equilibrium potential is $E_{\text{SHE}} = 0.72 \text{ V}$ (see Eq. (A.1)) vs a standard hydrogen electrode (SHE), and it is independent of pH of the solution. The potential corresponds to the horizontal line (2) in Fig. 1, where the potential scale vs $\text{Zn}^0/\text{Zn}^{2+}$ is shown for convenience. The obtained equilibrium potential $E_{\text{Zn}^0/\text{Zn}^{2+}} = E_{\text{SHE}} - (-0.76) \text{ V} \approx 1.5 \text{ V}$ for this reaction agrees well with the experimental average Zn^{2+} intercalation potential in MnO_2 [33]. Here -0.76 V [34, p. 536] is the standard reversible potential that corresponds to the half cell reaction $\text{Zn}(\text{s}) \longleftrightarrow \text{Zn}^{2+}(\text{aq}) + 2 \text{e}^-$. The calculated value of the equilibrium potential for reaction (2) has a small uncertainty (ca. 0.05 V, see hatched region in Fig. 1), which comes from two slightly different values of $\mu^\circ(\text{ZnMn}_2\text{O}_4)$ in Table I. The formation of hetaerolite is experimentally confirmed in Zn/EMD cells after discharge at 1.35 V vs $\text{Zn}^0/\text{Zn}^{2+}$ [12], which supports our diagram (Fig. 1).

Here we use pyrolusite ($\beta\text{-MnO}_2$) as a reference for $\mu^\circ(\text{MnO}_2)$ since it is the most stable natural form of MnO_2 . Other MnO_2 polymorphs are used in batteries, e.g., $\alpha\text{-MnO}_2$ [35]. The question is whether the structure of MnO_2 makes a significant difference to the Pourbaix

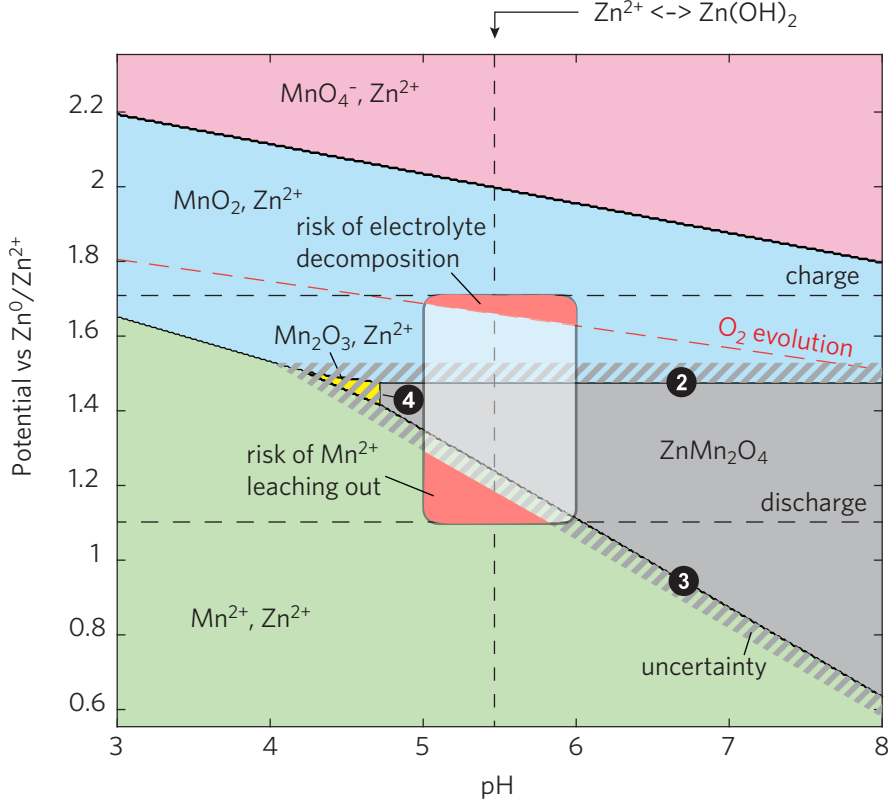
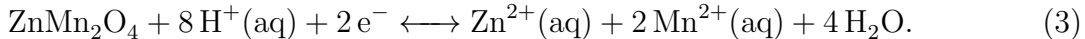


FIG. 1. Mn–Zn–H₂O Pourbaix diagram with ZnMn₂O₄ phase boundaries. The battery operating window is shown as a wide bar. The hatched area reflects the uncertainty in the stability region of ZnMn₂O₄ due to the uncertainty in its chemical potential (Table I). Phase boundaries marked with numbers are associated with the corresponding chemical reactions in the main text. The following concentrations of aqueous species are assumed [Mn²⁺] = 0.1 M, [Zn²⁺] = 2 M, and [MnO₄⁻] = 0.1 M.

diagram. We are not aware of any experimentally measured energy differences between α and β polymorphs but any differences can be inferred from DFT calculations. Our results suggest an energy difference of 0.05 eV/f.u. with β -MnO₂ having the lowest energy. Kitchaev *et al.* [36] came to a similar conclusion (ca. 0.07 eV/f.u.) with a more chemically accurate metha-GGA exchange correlation functional. If α -MnO₂ is used instead, the equilibrium potential for reaction (2) would increase by 0.05 V, which is not critical for the purpose of our discussion.

Now we turn to dissolution of the cathode material. It is expressed by the following

reaction:



The equilibrium potential for reaction (3) is $E_{\text{SHE}} = 1.78 \text{ V} - \text{pH} \times 0.237 \text{ V}$ (see Eq. (A.2)), which is a function of pH as the reaction involves both water and protons. The dissolution boundary is marked as (3) in Fig. 1 with the uncertainty as per the discussion above. Once we put this boundary in the context of the pH and potential range for Zn/MnO₂ battery operation (represented by a rectangle in Fig. 1), we immediately recognize that the lower boundary of ZnMn₂O₄ electrochemical stability is close to the lower boundary of the discharge potential. This result is in line with Li *et al.* [6] who attributed the capacity fade to a dissolution of the active cathode material into the electrolyte that takes place at lower voltages (less than 1.26 V vs Zn⁰/Zn²⁺). Tran *et al.* [12] reached a similar conclusion after experimental studies involving detection of soluble Mn²⁺ species formed during discharge, namely that Mn²⁺ is formed/dissolved at lower voltages (below $\sim 1.1 \text{ V}$ vs Zn⁰/Zn²⁺).

We can also see from the Pourbaix diagram in Fig. 1 that a more acidic electrolyte (i.e., lower pH) favours cathode dissolution (pH < 5). At the same time, pH is buffered by the formation of Zn(OH)₂ (pH > 5.5). This leaves us with a narrow pH range of $5 < \text{pH} < 5.5$ and a limited lowest discharge potential of $E_{\text{Zn}^0/\text{Zn}^{2+}}^{\text{min}} = 1.2 \text{ V}$ to avoid cathode corrosion.

To complete the map of ZnMn₂O₄ electrochemical stability, we also consider its transformation into Mn₂O₃



Here the transition occurs at a fixed pH = 4.75 (line (4) in Fig. 1) since the reaction does not involve electrons (see Eq. (A.3)). This pH boundary value is extremely sensitive to chemical potentials of species involved in the reaction. The Mn₂O₃ region can even vanish (see hatched zone in Fig. 1) with 0.1 eV uncertainty in $\mu^\circ(\text{ZnMn}_2\text{O}_4)$. This marks the pH boundary below which ZnMn₂O₄ is unstable and, thus, energy storage due to Zn²⁺ intercalation is not possible.

B. Chalcophanite

Chalcophanite (ZnMn₃O₇ · 3 H₂O) is a byproduct phase formed in the cathode material of rechargeable aqueous Zn/MnO₂ batteries upon cycling (see Sec. I). To understand the role of

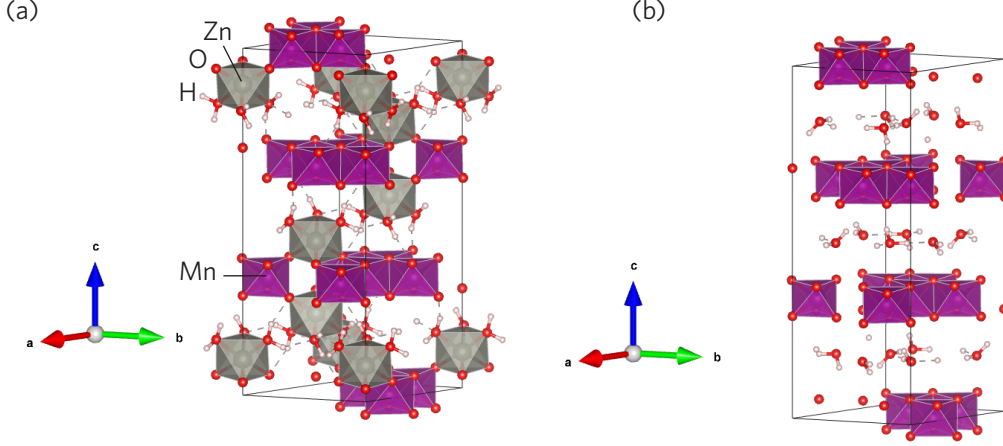


FIG. 2. (a) Chalcophanite $\text{ZnMn}_3\text{O}_7 \cdot 3\text{H}_2\text{O}$ and (b) chalcophanite with deintercalated zinc $\text{Mn}_3\text{O}_7 \cdot 3\text{H}_2\text{O}$.

$\text{ZnMn}_3\text{O}_7 \cdot 3\text{H}_2\text{O}$ in energy storage we begin with a review of its crystal structure, as shown in Fig. 2(a). The stoichiometry can be viewed as an $\text{Mn}_{0.86}\text{O}_2$ manganese-deficient layered structure where two Zn atoms electronically compensate for each Mn vacancy. At first glance, we can expect the chalcophanite phase to participate in the energy storage similar to ZnMn_2O_4 where Zn^{2+} can be deintercalated by an applied potential. The question that comes to mind is regarding the magnitude of the potential. If the thermodynamic properties of $\text{ZnMn}_3\text{O}_7 \cdot 3\text{H}_2\text{O}$ were experimentally determined, we would follow the same approach used in the analysis of reaction (2). However, in the absence of experimental data we can only rely on DFT calculations.

Aydinol *et al.* [37] proposed a method for calculation of an average Li intercalation voltage \bar{E} in transition metal oxides based on DFT total energies E . The original expression modified for the case of $\text{ZnMn}_3\text{O}_7 \cdot 3\text{H}_2\text{O}$ is

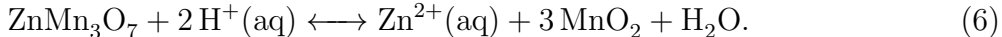
$$\bar{E}_{\text{Zn}^0/\text{Zn}^{2+}} = \frac{H(\text{Zn}_{x_1}\text{Mn}_3\text{O}_7 \cdot 3\text{H}_2\text{O}) + (x_2 - x_1)H(\text{Zn}) - H(\text{Zn}_{x_2}\text{Mn}_3\text{O}_7 \cdot 3\text{H}_2\text{O})}{2e(x_2 - x_1)}, \quad (5)$$

where $H(\text{Zn})$ is the DFT total energy of bulk Zn, e is the magnitude of the electron charge, and x_2 and x_1 are the effective number of Zn atoms in the structure before and after deintercalation ($x_1 < x_2$). The factor of two in the denominator reflects the ionic charge of Zn^{2+} . Our structural model of $\text{ZnMn}_3\text{O}_7 \cdot 3\text{H}_2\text{O}$ ($x_2 = 1$) is based on experimental data reported by Post and Appleman [38] (space group 148, $R\bar{3}$ hexagonal axes) with lattice parameters $a = b = 7.53 - 7.54$ and $c = 20.79 - 20.82$ Å. DFT lattice parameters $a = b = 7.54$ and

$c = 20.51 \text{ \AA}$ were obtained after full structural relaxation. The structure of $\text{Mn}_3\text{O}_7 \cdot 3\text{H}_2\text{O}$ ($x_1 = 0$) with deintercalated Zn (Fig. 2b) was obtained by removing Zn followed by full structural relaxation. The total energies of these two structures as well as the bulk Zn were used to calculate the intercalation potential using Eq. (5).

The DFT-predicted Zn intercalation potential in $\text{ZnMn}_3\text{O}_7 \cdot 3\text{H}_2\text{O}$ is $\bar{E}_{\text{Zn}^0/\text{Zn}^{2+}} = 2.6 \text{ V}$ vs $\text{Zn}^0/\text{Zn}^{2+}$. This is a very large value compared to 1.5 V for ZnMn_2O_4 . It should be noted that a DFT with PBE exchange-correlation functional always *underestimates* redox potentials relative to experiments due to its failure to properly capture correlation effects on the transition metal ion [39]. Such a large Zn intercalation potential in $\text{Zn}_{1/0}\text{Mn}_3\text{O}_7 \cdot 3\text{H}_2\text{O}$ can be attributed to the $\text{Mn}^{4+/5+}$ redox reaction instead of $\text{Mn}^{3+/4+}$ as in the case of $\text{Zn}_{1/0}\text{Mn}_2\text{O}_4$.

To add $\text{ZnMn}_3\text{O}_7 \cdot 3\text{H}_2\text{O}$ to the Pourbaix diagram we need to identify its boundaries of stability. This task is complicated by the lack of its experimental chemical potential, and DFT calculations are still too inaccurate for this purpose. Thus we assume $\mu^\circ(\text{ZnMn}_3\text{O}_7 \text{ hydr.}) = \mu^\circ(\text{ZnO hydr.}) + 3\mu^\circ(\text{MnO}_2) - \delta\mu$, where $\delta\mu$ is a stability margin which will be kept as a variable. First we investigate ZnMn_3O_7 decomposition with MnO_2 as one of the products



This reaction has no charge transfer and, thus, cannot be used for energy storage. The equilibrium boundary is at $\text{pH} = 5.32 - 0.118^{-1}\delta\mu$ ($\delta\mu$ should be in eV). Figure 3 presents the Pourbaix diagram with chalcophanite. The equilibrium boundary for this reaction, line (6), is included with the uncertainty region that reflects $\delta\mu = 0 - 0.1 \text{ eV}$. We believe that this is a correct order of magnitude for $\delta\mu$ as we did not observe chalcophanite experimentally at low pH values (see Sec. III D).

To map a boundary between chalcophanite and ZnMn_2O_4 we investigated the following reaction



that yields $E_{\text{SHE}} = 0.93 - \delta\mu/3\text{e} - 0.0395 \text{ pH}$ (line (7) in Fig. 3). Here $\delta\mu$ has a marginal influence on the result. At pH 5.5 the boundary will be at 0.71 V vs SHE or 1.47 V vs $\text{Zn}^0/\text{Zn}^{2+}$, which barely affects the ZnMn_2O_4 stability range.

It is now possible to rationalize experimental observations related to chalcophanite in Zn/MnO₂ cells and its relation to capacity fading. The region of $\text{ZnMn}_3\text{O}_7 \cdot 3\text{H}_2\text{O}$ electro-

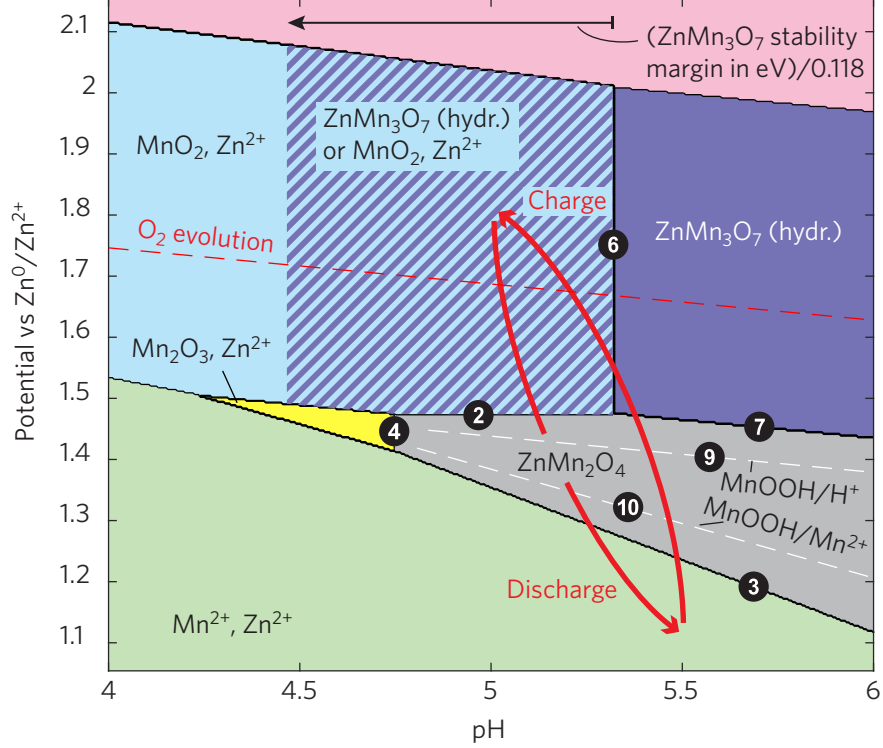


FIG. 3. Mn–Zn–H₂O Pourbaix diagram with boundaries for ZnMn₂O₄, ZnMn₃O₇ (hydr.), and MnOOH phases. The hatched region represent an uncertainty in ZnMn₃O₇ (hydr.) stability margin $\delta\mu = 0 - 0.1$ eV/f.u. A typical charge-discharge cycle of a Zn/MnO₂ cell is shown schematically. Phase boundaries marked with numbers are associated with the corresponding chemical reactions in the main text. The Zn(OH)₂ stability boundary at pH 5.45 is not shown. The following concentrations of aqueous species are assumed [Mn²⁺] = 0.1 M, [Zn²⁺] = 2 M, and [MnO₄⁻] = 0.1 M.

chemical stability on the Pourbaix diagram is in the location that was roughly outlined by Huang *et al.* [14] for Zn₂Mn₃O₈. Tran *et al.* [12] also observed formation of chalcophanite after charging of Zn/EMD cells and maintaining the potential at 1.8 V vs Zn⁰/Zn²⁺ (hatched region in Fig. 3) for 2 h. Most likely, reaction (6) is kinetically too slow and, instead, chalcophanite is deposited from dissolved aqueous species during battery charging [12] (hatched region in Fig. 3)



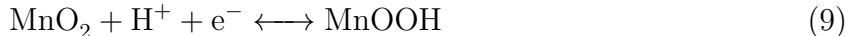
Here the presence of Mn²⁺(aq) in the electrolyte comes from the cathode material previously leached out during discharge, which explains the connection between chalcophanite forma-

tion and a deep discharge potential established by Li *et al.* [6]. Thus, chalcophanite acts as a scavenger in consuming dissolved $\text{Mn}^{2+}(\text{aq})$ species preventing them from depositing back as MnO_2 .

Here we have not conducted calculations on the $\text{Zn}_2\text{Mn}_3\text{O}_8$ compound since we do not have enough knowledge about its structure, thermodynamics, and experimental evidence for its importance in battery cycling performance. Also, we have not discussed zinc hydroxide sulfate $\text{Zn}_4(\text{OH})_6(\text{SO}_4) \cdot x\text{H}_2\text{O}$; the relevant Pourbaix diagram of $\text{Zn}-\text{S}-\text{H}_2\text{O}$ has been reported elsewhere [12].

C. H^+ -related energy storage mechanism

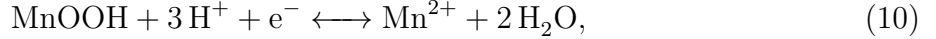
It is widely discussed in the literature [5, 6, 40, 41] that the proton exchange reaction



has a significant contribution to energy storage in Zn/MnO_2 aqueous cells. Interestingly, MnOOH was not included in the original $\text{Mn}-\text{H}_2\text{O}$ Pourbaix diagram [19], and its chemical potential was omitted. Bratsch [21] reported that $E^\circ = 0.98$ V for this reaction with $\beta\text{-MnO}_2$ at $\text{pH} = 0$, which translates into $\mu^\circ(\text{MnOOH}) = -5.81$ eV/f.u. (There is an alternative value of $\mu^\circ(\text{MnOOH})$ listed in Table I that indicates the amount of scatter in the experimental data.)

According to Eq. (A.6) the corresponding H^+ deintercalation potential in reaction (9) is $E_{\text{SHE}} = 0.98 - 0.0592 \text{pH}$ (in V), which amounts to $E_{\text{Zn}^0/\text{Zn}^{2+}} = 1.41$ V at $\text{pH} 5.5$. This potential is very close to $E_{\text{Zn}^0/\text{Zn}^{2+}} \approx 1.5$ V for the Zn^{2+} deintercalation reaction, as shown in Fig. 3 by lines (2) and (9). Magar *et al.* [42] arrived at the same result via DFT calculations, namely suggesting that proton insertion is only 0.1 eV less favourable than Zn^{2+} intercalation per MnO_2 formula unit. Since both energy mechanisms (Zn^{2+} and H^+ deintercalation) require nearly the same voltage, we can conclude that both can coexist and contribute to energy storage in the Zn/MnO_2 aqueous cell. Cyclic voltammetry [5] of Zn/MnO_2 cells also revealed two redox peaks upon both charge and discharge; the peaks were spaced 0.1–0.2 V apart (the same as our calculated equilibrium potentials for reactions (2) and (9) in Fig. 3) and are attributed to two redox reactions that involve $\text{Zn}^{2+}/\text{H}^+$ intercalation in MnO_2 .

MnOOH can also be further reduced to $\text{Mn}^{2+}(\text{aq})$



which takes place at $E_{\text{SHE}} = 1.52 - 0.178\text{pH}$ (in V) as shown in Fig. 3, line (10). At pH 5.5 this amounts to an equilibrium potential of $E_{\text{Zn}^0/\text{Zn}^{2+}} = 1.31$ V slightly above that for the ZnMn_2O_4 dissolution/reduction reaction (see line (3) in Fig. 3). This suggests that MnOOH is more susceptible to dissolution/reduction than ZnMn_2O_4 during discharge. Interestingly, 1.31 V is remarkably close to 1.26 V vs $\text{Zn}^0/\text{Zn}^{2+}$ which is marked as a boundary for capacity fade reactions by Li *et al.* [6].

D. Experimental validation

To validate the Zn–Mn–H₂O Pourbaix diagram in Fig. 3 we constructed a set of experiments that involve *ex situ* characterization of the electrolytic MnO₂ cathode material after cycling. Different regions of the Pourbaix diagram were sampled by changing the acidity of the electrolyte (pH 2.5 and 4). These pH values reflect the ‘as prepared’ electrolyte. During battery operation, the pH of the electrolyte evolves as a result of an increase in OH[−] concentration during discharge followed by zinc hydroxide sulphate (ZHS) precipitation that buffers the pH to ~ 5.5 [7, 13, 43]. When the initial pH of the electrolyte was 4, ZHS started to appear at potentials below 1.35 V but before 1.18 V. For the electrolyte with an initial pH of 2.5, ZHS formation was suppressed and did not occur until after a potential of 1.18 V was reached.

Morphological changes of EMD electrodes after 5 cycles in electrolytes with different pH values are shown in Fig. 4. For pH 4 (Fig. 4a), during discharge, the electrode surface is covered with ZHS flakes and a new layer of Zn-Mn oxide, consisting of hetaerolite and Zn-intercalated Mn oxide. During charge, ZHS disappears while the new Zn-Mn-oxide layer remains. For pH 2.5 (Fig. 4b), the morphology of the EMD electrode surface is retained with little or no change. During discharge, a small amount of ZHS forms and its formation is reversible during charge. In general, all EDX maps show that S signal overlaps with Zn; however, Zn has covered more of the electrode surface after cycling for the pH 4 solution than the pH 2.5 solution.

Pristine EMD has been characterized in Ref. 12. Briefly, the EMD powder is composed

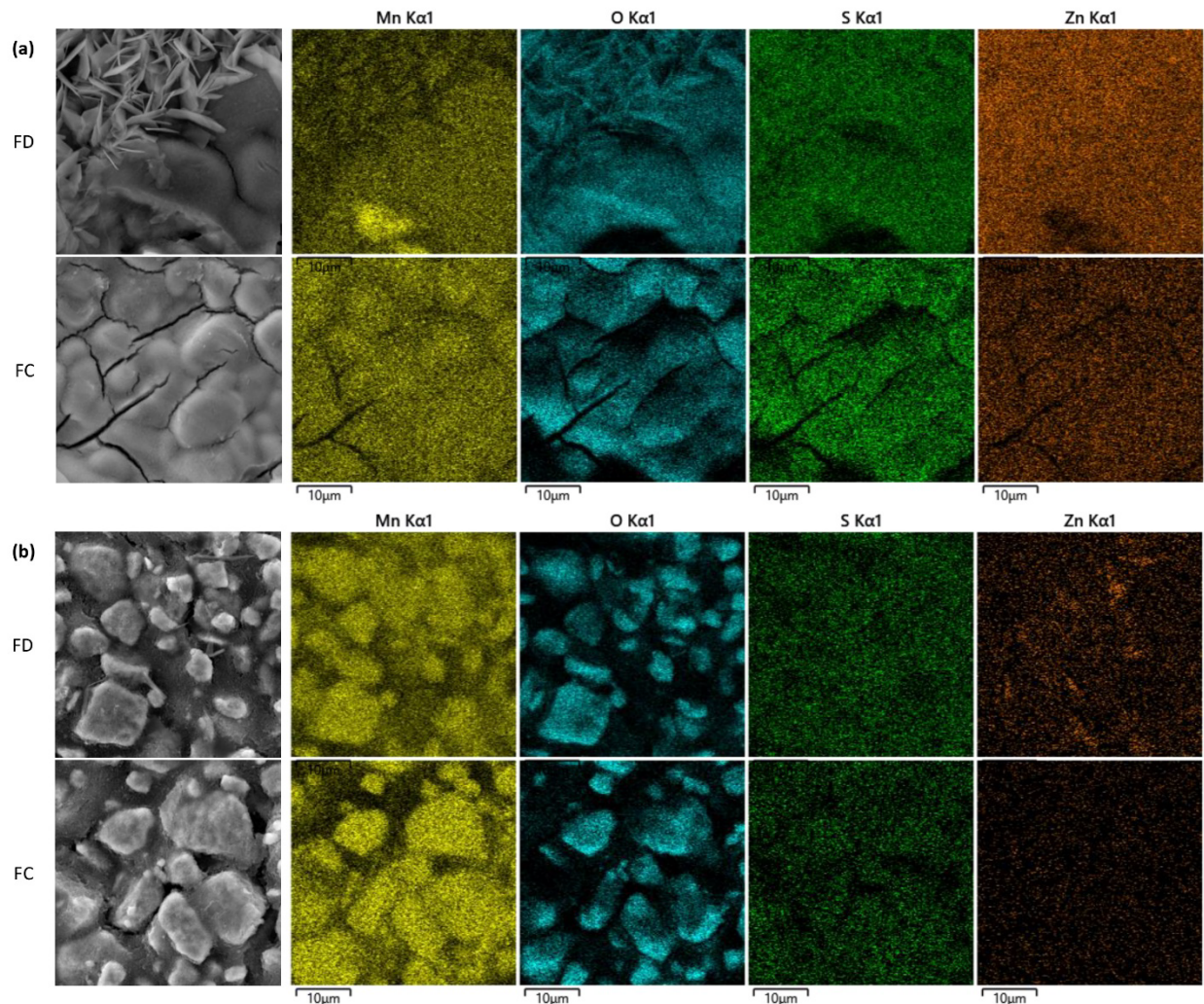


FIG. 4. SEM SE images and corresponding EDX maps of EMD electrodes after 5 cycles in electrolytes with different pH values: (a) pH 4 and (b) pH 2.5. Fully-discharged and fully-charged states are denoted as FD and FC, respectively.

of about 53% ϵ - MnO_2 , 34% ramsdellite, and 13% γ - MnO_2 , determined through Rietveld refinement. XRD results of EMD electrodes after 5 cycles are shown in Fig. 5. For both discharged electrodes, the major peak ((102) plane) for ϵ - MnO_2 at 56° shifts to a lower angle of 55.8° and 55.5° at pH 2.5 and 4, respectively. All other major ϵ - MnO_2 peaks ((100), (101) and (110), originally at 37.1° , 42.5° and 67.0° , respectively) also shift to lower angles during discharge. The (102) peak shifts back to 55.9° after charging, meaning that the structure of ϵ - MnO_2 can expand and collapse almost reversibly to accommodate Zn^{2+} ions. In addition, for the charged electrode cycled in the electrolyte with a pH of 4, a new

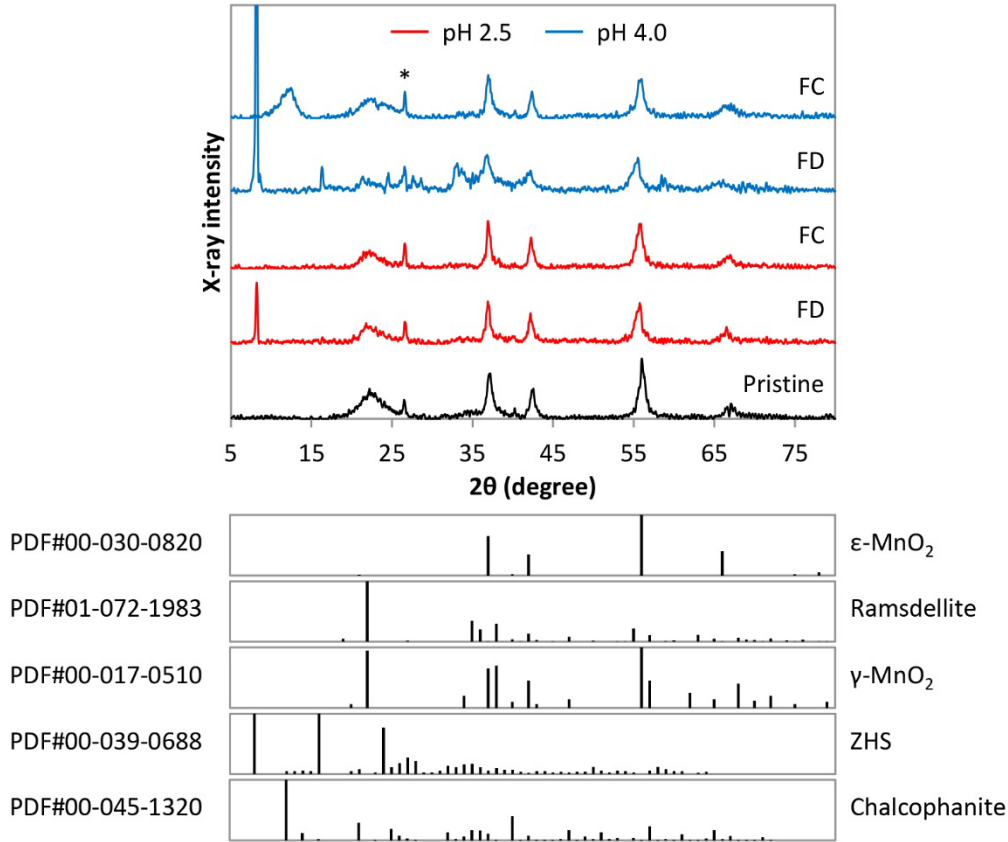


FIG. 5. XRD patterns of EMD electrodes after 5 cycles during GCD tests in electrolytes with different pH values. Reference PDF cards for ϵ -MnO₂, ramsdellite, γ -MnO₂, ZHS, and chalcophanite are included at the bottom of the XRD patterns. Fully-discharged and fully-charged states are denoted as FD and FC, respectively. The asterisk indicates a graphite peak from the current collector.

peak appears at 12.7° which matches the major peak for chalcophanite. This correlates well with the SEM images and EDX mapping of the Mn-Zn oxide layer that builds up on the EMD electrode surface during cycling in the electrolyte with pH 4. This result also matches the Pourbaix diagram (Fig. 3) with the pH buffering to 5.5 and a charge potential of 1.8 V vs $\text{Zn}^0/\text{Zn}^{2+}$. Chalcophanite is not observed for the electrolyte with pH 2.5, which is also expected from the Pourbaix diagram. The XRD results were not able to confirm the formation of hetaerolite (main peak is (211) at $\sim 36.5^\circ$) during discharge likely due to significant interference from both MnO₂ and ZHS peaks. However, the presence of hetaerolite was confirmed by electron diffraction in the TEM (Fig. 6(a)).

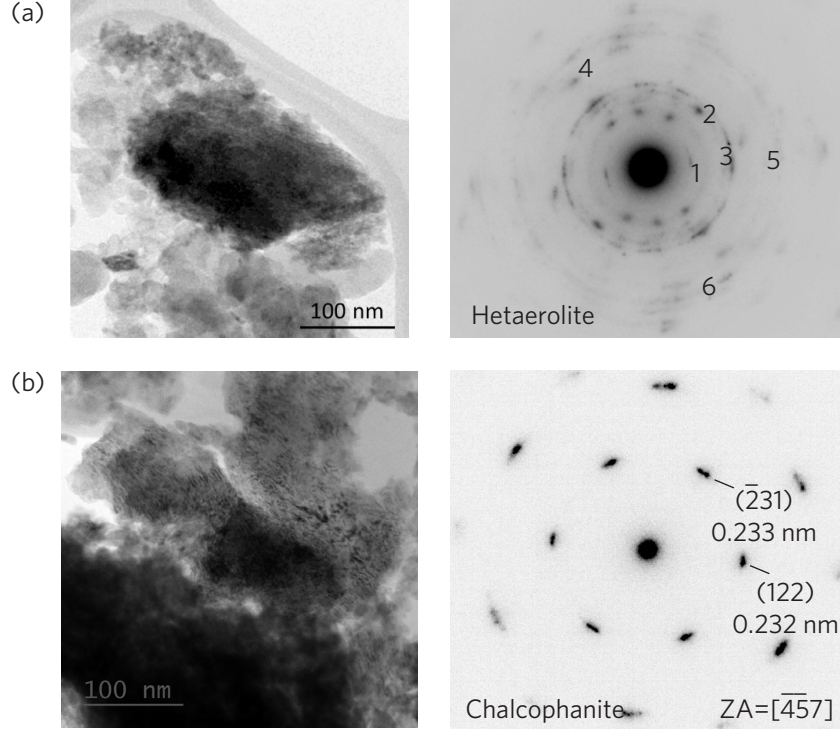


FIG. 6. TEM bright field images and SAED patterns from the EMD electrodes at different stages during cycling at pH 4. (a) Electrode discharged at 1.35 V during the 1st cycle and (b) fully charged electrode held for 2 h at 1.8 V during the 50th cycle. The labels 1–6 on the SAED pattern for hetaerolite correspond to the d-spacings, in order, in Table II.

According to Chamoun *et al.* [7], hetaerolite should not form if the EMD electrode is cycled in a more acidic electrolyte. Thus, only electrodes discharged at 1.35 V during the 1st cycle and fully charged at 1.8 V for 2 h during the 50th cycle in pH 4 are shown in Fig. 6, including examples of SAED patterns from the particles shown. It should be noted that when Zn/MnO₂ batteries discharge, the pH of the electrolyte in the vicinity of the EMD electrodes should increase significantly. The SAED patterns in Fig. 6a and b were indexed to hetaerolite (ZnMn₂O₄) (Table II) and chalcophanite (ZnMn₃O₇), respectively. These results agree with the Pourbaix diagram in Fig. 3.

IV. CONCLUSIONS

We have presented a refined Mn–Zn–H₂O Pourbaix diagram with emphasis on the battery-relevant range of parameters (pH 4 – 6, $E_{\text{Zn}^0/\text{Zn}^{2+}} = 1.1 - 1.8$ V). The diagram

TABLE II. Indexed d-spacings for the SAED pattern in Figure 6a and d-spacings from the PDF card for hetaerolite (PDF#01-077-0407).

d-spacing (Å)	Hetaerolite	(<i>hkl</i>)
4.84	4.86	(101)
2.72	2.71	(103)
2.47	2.46	(211)
1.81	1.80	(204)
1.57	1.56	(321)
1.54	1.52	(224)

maps out boundaries of electrochemical stability for MnO_2 , ZnMn_2O_4 , ZnMn_3O_7 , and MnOOH . The diagram helps to rationalize experimental observation of processes and phases occurring during the charge/discharge of Zn/MnO_2 aqueous cells. The average charge potential of 1.5 V vs $\text{Zn}^0/\text{Zn}^{2+}$ and the mid potential value of the redox couple peaks (~ 1.4 V vs $\text{Zn}^0/\text{Zn}^{2+}$) measured during cyclic voltammetry agree with the boundaries between ZnMn_2O_4 and MnO_2 for Zn^{2+} intercalation ($E_{\text{Zn}^0/\text{Zn}^{2+}} = 1.5$ V) or the boundary between MnOOH and MnO_2 for H^+ intercalation ($E_{\text{Zn}^0/\text{Zn}^{2+}} = 1.4$ V at pH 5.5). The experimentally observed capacity fade attributed to dissolution of ZnMn_2O_4 or MnOOH at low discharge potentials (below 1.1 – 1.2 V vs $\text{Zn}^0/\text{Zn}^{2+}$) agrees with boundaries between these phases and aqueous Mn^{2+} ($E_{\text{Zn}^0/\text{Zn}^{2+}} \approx 1.2$ V at pH 5.5). The precipitation of chalcophanite ZnMn_3O_7 in a cathode material charged at 1.8 V correlates with its predicted range of stability above $E_{\text{Zn}^0/\text{Zn}^{2+}} \approx 1.5$ V at pH 5.5. Chalcophanite (formed at high voltages during charge) participates in capacity fade by consuming dissolved Mn^{2+} species and preventing their return back to MnO_2 . Unlike ZnMn_2O_4 , it is not feasible to deintercalate Zn^{2+} from ZnMn_3O_7 .

The impact of electrolyte pH has been investigated experimentally for aqueous zinc-ion batteries. For an electrolyte with pH 4, a fraction of pristine EMD transforms to hetaerolite and chalcophanite during discharge and charge, respectively. The transformation does not occur when the pH of electrolyte is adjusted to 2.5, which validates the proposed $\text{Mn-Zn-H}_2\text{O}$ Pourbaix diagram.

Making progress in understanding the reaction mechanisms responsible for capacity fade

can provide insight to future researchers working on performance improvements to MnO_2 type cathodes. In addition, the electrochemical stability should be used as an additional design criterion in exploration of future cathode materials for aqueous rechargeable batteries.

ACKNOWLEDGMENTS

This work was supported by the Salient Energy, the NSERC Alliance program, the Mitacs Globalink program, the International Manganese Institute (IMnI) and a grant through the Mitacs Accelerate program (FR49801).

-
- [1] L. E. Blanc, D. Kundu, and L. F. Nazar, Scientific challenges for the implementation of Zn-ion batteries, *Joule* **4**, 771 (2020).
 - [2] T. Shoji, M. Hishinuma, and T. Yamamoto, Zinc-manganese dioxide galvanic cell using zinc sulphate as electrolyte. Rechargeability of the cell, *J. Appl. Electrochem.* **18**, 521 (1988).
 - [3] C. Xu, B. Li, H. Du, and F. Kang, Energetic zinc ion chemistry: The rechargeable zinc ion battery, *Angew. Chem. Int. Ed.* **51**, 933 (2011).
 - [4] W. Sun, F. Wang, S. Hou, C. Yang, X. Fan, Z. Ma, T. Gao, F. Han, R. Hu, M. Zhu, and C. Wang, Zn/MnO₂ battery chemistry with H⁺ and Zn²⁺ coinsertion, *J. Am. Chem. Soc.* **139**, 9775 (2017).
 - [5] Q. Zhao, X. Chen, Z. Wang, L. Yang, R. Qin, J. Yang, Y. Song, S. Ding, M. Weng, W. Huang, J. Liu, W. Zhao, G. Qian, K. Yang, Y. Cui, H. Chen, and F. Pan, Unravelling H⁺/Zn²⁺ synergistic intercalation in a novel phase of manganese oxide for high-performance aqueous rechargeable battery, *Small* **15**, 1904545 (2019).
 - [6] Y. Li, S. Wang, J. R. Salvador, J. Wu, B. Liu, W. Yang, J. Yang, W. Zhang, J. Liu, and J. Yang, Reaction mechanisms for long-life rechargeable Zn/MnO₂ batteries, *Chem. Mater.* **31**, 2036 (2019).
 - [7] M. Chamoun, W. R. Brant, C.-W. Tai, G. Karlsson, and D. Noréus, Rechargeability of aqueous sulfate Zn/MnO₂ batteries enhanced by accessible Mn²⁺ ions, *Energy Stor. Mater.* **15**, 351 (2018).
 - [8] B. Lee, C. S. Yoon, H. R. Lee, K. Y. Chung, B. W. Cho, and S. H. Oh, Electrochemically-

- induced reversible transition from the tunneled to layered polymorphs of manganese dioxide, *Sci. Rep.* **4**, 6066 (2014).
- [9] H. Pan, Y. Shao, P. Yan, Y. Cheng, K. S. Han, Z. Nie, C. Wang, J. Yang, X. Li, P. Bhattacharya, K. T. Mueller, and J. Liu, Reversible aqueous zinc/manganese oxide energy storage from conversion reactions, *Nat. Energy* **1**, 16039 (2016).
- [10] M. H. Alfaruqi, S. Islam, D. Y. Putro, V. Mathew, S. Kim, J. Jo, S. Kim, Y.-K. Sun, K. Kim, and J. Kim, Structural transformation and electrochemical study of layered MnO_2 in rechargeable aqueous zinc-ion battery, *Electrochimica Acta* **276**, 1 (2018).
- [11] D. Chao, W. Zhou, C. Ye, Q. Zhang, Y. Chen, L. Gu, K. Davey, and S.-Z. Qiao, An electrolytic Zn-MnO_2 battery for high-voltage and scalable energy storage, *Angew. Chem. Int. Ed.* **58**, 7823 (2019).
- [12] T. N. T. Tran, S. Jin, M. Cuisinier, B. D. Adams, and D. G. Ivey, Reaction mechanisms for electrolytic manganese dioxide in rechargeable aqueous zinc-ion batteries, *Sci. Rep.* **11**, 20777 (2021).
- [13] C. F. Bischoff, O. S. Fitz, J. Burns, M. Bauer, H. Gentischer, K. P. Birke, H.-M. Henning, and D. Biro, Revealing the local pH value changes of acidic aqueous zinc ion batteries with a manganese dioxide electrode during cycling, *J. Electrochem. Soc.* **167**, 020545 (2020).
- [14] Y. Huang, J. Mou, W. Liu, X. Wang, L. Dong, F. Kang, and C. Xu, Novel insights into energy storage mechanism of aqueous rechargeable Zn/MnO_2 batteries with participation of Mn^{2+} , *Nano-Micro Letters* **11**, 49 (2019).
- [15] A. Jain, G. Hautier, S. P. Ong, C. J. Moore, C. C. Fischer, K. A. Persson, and G. Ceder, Formation enthalpies by mixing GGA and GGA + U calculations, *Phys. Rev. B* **84**, 045115 (2011).
- [16] K. A. Persson, B. Waldwick, P. Lazic, and G. Ceder, Prediction of solid-aqueous equilibria: Scheme to combine first-principles calculations of solids with experimental aqueous states, *Phys. Rev. B* **85**, 235438 (2012).
- [17] Z. Zeng, M. K. Y. Chan, Z.-J. Zhao, J. Kubal, D. Fan, and J. Greeley, Towards first principles-based prediction of highly accurate electrochemical Pourbaix diagrams, *J. Phys. Chem. C* **119**, 18177 (2015).
- [18] Z. Wang, X. Guo, J. Montoya, and J. K. Nørskov, Predicting aqueous stability of solid with computed Pourbaix diagram using SCAN functional, *npj Comput. Mater.* **6**, 160 (2020).

- [19] M. Pourbaix, *Atlas of electrochemical equilibria in aqueous solutions*, 2nd ed. (National Association of Corrosion Engineers, 1974).
- [20] K. T. Jacob, A. Kumar, G. Rajitha, and Y. Waseda, Thermodynamic data for Mn_3O_4 , Mn_2O_3 and MnO_2 , *High Temp. Mater. Processes (London)* **30**, 459 (2011).
- [21] S. G. Bratsch, Standard electrode potentials and temperature coefficients in water at 298.15 K, *J. Phys. Chem. Ref. Data* **18**, 1 (1989).
- [22] C. G. Maier, G. S. Parks, and C. T. Anderson, The free energy of formation of zinc oxide, *J. Am. Chem. Soc.* **48**, 2564 (1926).
- [23] J. D. Hem, C. E. Roberson, and C. J. Lind, Synthesis and stability of hetaerolite, ZnMn_2O_4 , at 25°C, *Geochim. Cosmochim. Acta* **51**, 1539 (1987).
- [24] P. Hohenberg and W. Kohn, Inhomogeneous electron gas, *Phys. Rev.* **136**, B864 (1964).
- [25] W. Kohn and L. J. Sham, Self-consistent equations including exchange and correlation effects, *Phys. Rev.* **140**, A1133 (1965).
- [26] G. Kresse and J. Furthmüller, Efficient iterative schemes for ab initio total-energy calculations using a plane-wave basis set, *Phys. Rev. B* **54**, 11169 (1996).
- [27] G. Kresse and D. Joubert, From ultrasoft pseudopotentials to the projector augmented-wave method, *Phys. Rev. B* **59**, 1758 (1999).
- [28] P. E. Blöchl, Projector augmented-wave method, *Phys. Rev. B* **50**, 17953 (1994).
- [29] J. P. Perdew, K. Burke, and M. Ernzerhof, Generalized gradient approximation made simple, *Phys. Rev. Lett.* **77**, 3865 (1996).
- [30] S. Grimme, J. Antony, S. Ehrlich, and H. Krieg, A consistent and accurate ab initio parametrization of density functional dispersion correction (DFT-D) for the 94 elements H-Pu, *J. Chem. Phys.* **132**, 154104 (2010).
- [31] H. J. Monkhorst and J. D. Pack, Special points for Brillouin-zone integrations, *Phys. Rev. B* **13**, 5188 (1976).
- [32] B. D. Adams, J. H. Ahn, R. D. Brown, R. D. Clarke, M. Cuisinier, and J. P. S. Lee, Secondary electrochemical cell having a zinc metal negative electrode and mild aqueous electrolyte and methods thereof (2019), patent WO/2019/095075.
- [33] P. Canepa, G. S. Gautam, D. C. Hannah, R. Malik, M. Liu, K. G. Gallagher, K. A. Persson, and G. Ceder, Odyssey of multivalent cathode materials: Open questions and future challenges, *Chem. Rev.* **117**, 4287 (2017).

- [34] J. Brady and G. E. Humiston, *General chemistry, principles and structure* (John Wiley & Sons, New York, 1982).
- [35] M. H. Alfaruqi, J. Gim, S. Kim, J. Song, J. Jo, S. Kim, V. Mathew, and J. Kim, Enhanced reversible divalent zinc storage in a structurally stable α -MnO₂ nanorod electrode, *J. Power Sources* **288**, 320 (2015).
- [36] D. A. Kitchaev, H. Peng, Y. Liu, J. Sun, J. P. Perdew, and G. Ceder, Energetics of MnO₂ polymorphs in density functional theory, *Phys. Rev. B* **93**, 045132 (2016).
- [37] M. K. Aydinol, A. F. Kohan, G. Ceder, K. Cho, and J. Joannopoulos, Ab initio study of lithium intercalation in metal oxides and metal dichalcogenides, *Phys. Rev. B* **56**, 1354 (1997).
- [38] J. E. Post and D. E. Appleman, Chalcophanite, ZnMn₃O₇ · 3H₂O; new crystal-structure determinations, *Am. Mineral.* **73**, 1401 (1988).
- [39] V. L. Chevrier, S. P. Ong, R. Armiento, M. K. Y. Chan, and G. Ceder, Hybrid density functional calculations of redox potentials and formation energies of transition metal compounds, *Phys. Rev. B* **82**, 075122 (2010).
- [40] S. Wen, J.-W. Lee, I.-H. Yeo, J. Park, and S. il Mho, The role of cations of the electrolyte for the pseudocapacitive behavior of metal oxide electrodes, MnO₂ and RuO₂, *Electrochim. Acta* **50**, 849 (2004).
- [41] P. Oberholzer, E. Tervoort, A. Bouzid, A. Pasquarello, and D. Kundu, Oxide versus nonoxide cathode materials for aqueous Zn batteries: An insight into the charge storage mechanism and consequences thereof, *ACS Appl. Mater. Interfaces* **11**, 674 (2018).
- [42] B. A. Magar, N. Paudel, T. N. Lambert, and I. Vasiliev, Ab initio studies of discharge mechanism of MnO₂ in deep-cycled rechargeable Zn/MnO₂ batteries, *J. Electrochem. Soc.* **167**, 020557 (2020).
- [43] B. Lee, H. R. Seo, H. R. Lee, C. S. Yoon, J. H. Kim, K. Y. Chung, B. W. Cho, and S. H. Oh, Critical role of pH evolution of electrolyte in the reaction mechanism for rechargeable zinc batteries, *ChemSusChem* **9**, 2948 (2016).

Appendix: Thermodynamic calculations of equilibrium potentials

Here we show a detailed workflow to illustrate calculations of the equilibrium potential for the electrochemical reaction using thermodynamic data from Table I and assuming con-

centrations of aqueous species at 2 M for Zn^{2+} and 0.1 M for Mn^{2+} . Results are shown for the reaction (2)

$$\begin{aligned}\mu(\text{Zn}^{2+}, \text{aq}) + 2\mu^\circ(\text{MnO}_2) + 2\mu(e^-) &= \mu^\circ(\text{ZnMn}_2\text{O}_4) \\ -11.17 \text{ eV} - 2e E_{\text{SHE}} &= -12.61 \text{ eV} \\ E_{\text{SHE}} &= 0.72 \text{ V},\end{aligned}\tag{A.1}$$

reaction (3)

$$\begin{aligned}\mu(\text{Zn}^{2+}, \text{aq}) + 2\mu(\text{Mn}^{2+}, \text{aq}) + 4\mu^\circ(\text{H}_2\text{O}) &= \mu^\circ(\text{ZnMn}_2\text{O}_4) + 8\mu(\text{H}^+, \text{aq}) + 2\mu(e^-) \\ -16.18 \text{ eV} &= -12.61 \text{ eV} - \text{pH} \times 0.476 \text{ eV} - 2e E_{\text{SHE}} \\ E_{\text{SHE}} &= 1.78 \text{ V} - \text{pH} \times 0.237 \text{ V},\end{aligned}\tag{A.2}$$

reaction (4)

$$\begin{aligned}\mu(\text{Zn}^{2+}, \text{aq}) + \mu^\circ(\text{Mn}_2\text{O}_3) + \mu^\circ(\text{H}_2\text{O}) &= \mu^\circ(\text{ZnMn}_2\text{O}_4) + 2\mu(\text{H}^+) \\ -13.17 \text{ eV} &= -12.61 \text{ eV} - 0.118 \text{ eV} \times \text{pH} \\ \text{pH} &= 4.75,\end{aligned}\tag{A.3}$$

reaction (6)

$$\begin{aligned}\mu^\circ(\text{ZnMn}_3\text{O}_7 \text{ hydr.}) + 2\mu(\text{H}^+) &= \mu(\text{Zn}^{2+}, \text{aq}) + 3\mu^\circ(\text{MnO}_2) + \mu^\circ(\text{H}_2\text{O}) \\ -17.83 \text{ eV} - \delta\mu - 0.118 \text{ eV} \times \text{pH} &= -18.46 \text{ eV} \\ \text{pH} &= 5.32 - \frac{\delta\mu \text{ (eV)}}{0.118},\end{aligned}\tag{A.4}$$

reaction (7)

$$\begin{aligned}3\mu^\circ(\text{ZnMn}_2\text{O}_4) + 2\mu^\circ(\text{H}_2\text{O}) &= 2\mu^\circ(\text{ZnMn}_3\text{O}_7) + \mu(\text{Zn}^{2+}, \text{aq}) + 4\mu(\text{H}^+) + 6\mu(e^-) \\ -42.75 \text{ eV} &= -37.16 \text{ eV} - 2\delta\mu - 0.237 \text{ eV} \times \text{pH} - 6e E_{\text{SHE}} \\ E_{\text{SHE}} &= 0.93 - \delta\mu/3e - \text{pH} \times 0.0395 \text{ V},\end{aligned}\tag{A.5}$$

reaction (9)

$$\begin{aligned}\mu^\circ(\text{MnO}_2) + \mu(\text{H}^+, \text{aq}) + \mu(e^-) &= \mu^\circ(\text{MnOOH}) \\ -4.83 \text{ eV} - \text{pH} \times 0.0592 \text{ eV} - e E_{\text{SHE}} &= -5.81 \text{ eV} \\ E_{\text{SHE}} &= 0.98 - \text{pH} \times 0.0592 \text{ V},\end{aligned}\tag{A.6}$$

reaction (10)

$$\begin{aligned}\mu^\circ(\text{MnOOH}) + 3\mu(\text{H}^+) + \mu(\text{e}^-) &= \mu(\text{Mn}^{2+}, \text{aq}) + 2\mu^\circ(\text{H}_2\text{O}) \\ -5.81 \text{ eV} - \text{pH} \times 0.178 \text{ eV} - eE_{\text{SHE}} &= -7.33 \text{ eV} \\ E_{\text{SHE}} &= 1.52 - \text{pH} \times 0.178 \text{ V}.\end{aligned}\tag{A.7}$$